LA-UR-02-1633
*Approved for public release;
distribution is unlimited.*

Title:	**Comparisons Between Hyperspectral Passive and Multispectral Active Sensor Measurements**
Author(s):	B.R. Foy, R.R. Petrin, C.R. Quick, T. Shimada, and J.J. Tiee
Submitted to:	
	http://lib-www.lanl.gov/cgi-bin/getfile?00937144.pdf

Comparisons Between Hyperspectral Passive
and Multispectral Active Sensor Measurements

B.R. Foy,* R.R. Petrin, C.R. Quick, T. Shimada, J.J. Tiee
Los Alamos National Laboratory

ABSTRACT

We conducted experiments with side-by-side active and passive sensors in the 8-12 micron region in order to study similarities and differences in the spectral signatures detected by the two sensors. The active instrument was a frequency-agile CO_2 lidar system operating on 44 wavelengths and at a total pulse repetition rate of 5 kHz. The passive system was an Aerospace Corp. dispersive imaging spectrometer with 128 spectral channels from 750-1250 cm^{-1}. The sensors viewed both natural scenes and man-made objects typical of industrial scenes at ranges of 1-3 km along horizontal paths. Scenes were viewed under various ambient conditions in order to evaluate the effects of radiance contrast for the passive images at different times of a day. Both imaging and "staring" experiments were conducted on the background scenes. An imaging Fabry-Perot spectrometer was also deployed to provide single-wavelength snapshots of scenes at several selected wavelengths. We present details of the experiments and preliminary analysis of the data that show how reflectance data (from an active sensor) can be compared to passive data (influenced by ground emissivity, atmospheric radiance, and temperature differences) in scenes with a significant level of "clutter".

Keywords: Hyperspectral imaging, lidar, infrared imaging, clutter, image classification, temperature-emissivity separation

1. INTRODUCTION

Hyperspectral imaging is widely used as a passive remote sensing tool in both airborne and ground-based applications for scene characterization, atmospheric measurements, chemical plume detection, and remote materials characterization. Lidar, or active remote sensing techniques can also be used in remote chemical detection. Scene imaging by lidar is a feasible means of mapping objects in a scene through reflectivity rather than radiance, but it has not been very widely adopted. We have been interested in developing passive and active approaches for remote sensing, as well as "hybrid" approaches that may make use of both types of data. In the "long-wave" infrared (LWIR, 8-12 μm), passive sensors detect the radiance spectrum of various objects in a scene, which is amplified by both increasing temperature and emissivity. Lidar sensors detect the intrinsic reflectivity of objects. Both passive and active sensors detect a spectral signature that is multiplied by atmospheric transmission along the line of sight. Passive sensors have the additional complication that the same atmospheric path makes a radiance contribution. Hence the ability to detect objects and chemicals by a passive sensor is regulated by radiance contrast.[1-7] On the other hand, active sensor measurements are limited by laser speckle noise.[8]

Given the physical difference between passive and active measurement approaches, it may be possible to combine them in order to take advantage of complementary characteristics and to effect a separation between temperature and emissivity in the passively detected information. There have been some previous examples of active-passive hybrid approaches.[9,10] To our knowledge, however, these efforts have been limited to single-wavelength active approaches, coupled with either broadband passive or multispectral passive measurements. In this paper, we report experimental results using a multispectral active sensor coupled with a hyperspectral passive sensor. Both sensors yield detailed spectroscopic properties of objects and the atmosphere, and both were used in imaging and staring modes. We present preliminary results of these detailed experiments. We first outline an argument for the importance of radiance contrast in passive measurements.

2. RADIANCE CONTRAST AND CHEMICAL CONTRAST

Consider a passive sensor that is either looking down at the ground or looking horizontally through the atmosphere at a radiating object. In order for the sensor to detect a chemical plume, the radiance contrast between plume and ground must be nonzero. This well-known effect has been noted in published experimental results,[1] and has been discussed in the context of performance modeling,[2-7] but it apparently has not been discussed extensively in the context of scene clutter in a passive imaging sensor. The detection sensitivity of the instrument is essentially linearly proportional to the radiance contrast, as shown below. This quantity is a function of the temperature difference between plume and ground, the emissivity of the ground, and the spectral shape of both the chemical absorption and the object's spectral albedo. In typical cluttered scenes, plume contrast varies from pixel to pixel. Hence even a perfectly uniform plume will be modulated by ground clutter, which has an impact on the chemical detection limit for the sensor. Detection may be improved by independent knowledge of object spectral emittances in the scene, object temperatures, or both. A lidar system could help to provide this additional information. We first consider how ground clutter modulates the chemical signature in the passive sensor data.

The importance of plume contrast is readily apparent when one writes down the expression for total radiance detected by the passive sensor. This is a sum of photons emitted by the plume, the ground beneath the plume, the atmosphere, and noise sources:

$$R(v_j) = R^p(v_j) + R^g(v_j) + R^\uparrow(v_j) + N(v_j) \qquad (1)$$

where $R(v_j)$ represents the calibrated radiance that a sensor measures from one scene pixel at a spectral bin j. The plume radiance term, $R^p(v_j)$ is given by

$$R^p(v_j) = c_p l_p \alpha_p(v_j)\left[L^b(v_j, T_p) - \varepsilon(v_j)L^b(v_j, T_g)\right]\tau(v_j) \qquad (2)$$

and the ground radiance by

$$R^g(v_j) = \varepsilon(v_j)L^b(v_j, T_g)\tau(v_j) \qquad (3)$$

where we have neglected the reflected downwelling radiation from the atmosphere (which is small in the LWIR). Here, L is the Planck blackbody function,

$$L^b(v_j, T) = \frac{c_1 v_j^3}{e^{hv_j/kT} - 1} \quad \left(\frac{W}{cm^2 \cdot sr \cdot cm^{-1}}\right) \qquad (4)$$

symbols p and g refer to plume and ground, τ is the atmospheric transmission between radiation source and sensor, $c_p l_p$ is the product of chemical concentration and plume thickness, α is the chemical absorption coefficient, and ε is the emissivity spectrum of the ground. Eqn. (2) is a statement that the observed radiance from the plume is a combination of photons emitted by the chemical and photons emitted by the ground below the plume, which are partially absorbed by the plume. (An optically thin plume is assumed.) The net SNR with which a passive sensor sees a chemical depends (in part) on this radiance difference, divided by the ground radiance given by (3). This corresponds to on-plume/off-plume comparison of pixels in an image. We shall define that ratio as the chemical contrast K:

$$K(v, T_p) = c_p l_p \alpha(v)\frac{L(v, T_p) - \varepsilon(v)L(v, T_g)}{\varepsilon(v)L(v, T_g)} = c_p l_p \alpha(v) \times C_R(v) \qquad (5)$$

This contrast function is made up of the chemical absorption multiplied by the "radiance contrast" C_R. The atmospheric transmission $\tau(v)$ cancels out in the ratio because it is approximately the same in both (2) and (3), provided that the plume is close to the ground. The chemical contrast, a dimensionless quantity, is spectrally dependent through not just the spectral dependence of the chemical, $\alpha(v)$, but through the spectral emittance of the ground $\varepsilon(v)$. (There is an additional mild spectral dependence from the Planck function.) Eqn. (5) has approximate forms that are often used

instead of the full expression. Generally, $T_g \sim 300$ K and $T_p - T_g$ is small (-5 to +10 K)[11], in cases where the plume temperature is close to the ambient air temperature. In that case, the chemical contrast simplifies to

$$K(\nu, T_p) \approx c_p l_p \frac{\alpha(\nu)}{\varepsilon(\nu)}\left[\frac{h\nu}{kT_g}\frac{T_p - T_g}{T_p} + 1 - \varepsilon(\nu)\right] \qquad (6)$$

For most materials, the emissivity in the LWIR is close to unity (0.9 to 0.99). In addition, it typically varies slowly with wavelength, at least in the region where the chemical absorbs. It is common to set $\varepsilon = 1$ and adjust the ground temperature to make up the difference in the resulting radiance, i.e to use the brightness temperature T_B of the ground. Now we have the even simpler expression

$$K(\nu, \Delta T_B) \approx c_p l_p \alpha(\nu)\left[\frac{h\nu}{kT_B}\frac{\Delta T_B}{T_B}\right] = c_p l_p \alpha(\nu) \times C_B \qquad (7)$$

where ΔT_B is interpreted as the "plume-ground brightness temperature difference." The quantity C_B is the "radiance contrast factor," which is a wavelength-independent approximation of the full radiance contrast expression $C_R(\nu)$. "Chemical contrast" includes C_B together with the chemical part of the plume signature. Equation (7) is a convenient approximation that allows one to estimate the effect of radiance contrast on the detectability of a plume without evaluating the full Planck function. The chemical detection SNR is comprised of instrumental SNR multiplied by K. However, one must use suitable values for ΔT_B and T_B. In a cluttered scene, these actually change from pixel to pixel as the material composition changes, so that one must find some average value of the brightness temperature. We now consider the impact of substituting the approximate form (7) for the full expression (5). In other words, we will assess the impact of including the spectral dependence of the radiance contrast.

The radiance contrast $C_R(\nu)$ depends on plume-ground temperature difference and the spectral albedo of the ground. It takes values of –1 when $T_p \ll T_g$ (equation 5) and is positive when $T_p > T_g$. A typical value is obtained from $\lambda = 10$ μm, $T_B = 300$ K, and $\Delta T_B = 5$ K, for which $C_B = 0.08$. In these conditions the chemical SNR is 0.08 times the raw photon SNR. This phenomenon has been recognized by previous authors.[1-7] Flanigan[4], in particular, shows calculated results for chemical detection limit at varying ΔT_B. At exactly zero plume contrast, even large amounts of chemical are undetectable by the passive sensor even though, paradoxically, plume photons may be detected as photoelectrons. On the other hand, in hot plumes with large values of plume contrast, even low concentrations can be detected, a passive sensor advantage that active sensors do not have.

Note that in going from Eq. 6 to Eq. 7, we have made the substitution: $\dfrac{\Delta T_B}{T_B^{\,2}} = \dfrac{T_p - T_g}{T_g T_p}$ and we have used $T_p \approx T_g$. The

plume-ground brightness temperature difference and T_B are essentially defined by this expression; rigorous definitions in terms of physical temperatures and emissivity are somewhat more complicated.

Returning to Eqn. (5), we see that for a given chemical and a given ground material, there is a plume-ground temperature difference at which cancellation occurs and the chemical cannot be detected at any concentration. This is the zero-contrast condition. Actually, complete cancellation only occurs at selected wavelengths, whereas other wavelengths will be non-zero. But in a multiple regression least-squares fit of the known spectrum to the data, some features will be positive and some negative, producing an estimate of zero for the concentration. (It is interesting to ask whether a non-standard regression analysis could incorporate features of both signs at different wavelengths, but that is beyond the scope of this analysis). Chemical contrast is depicted graphically for a simple case in Fig. 1, which shows plots of the contrast function $K(\nu, T_p)$ at different plume temperatures. In this example, the chemical Freon 113 is detected against a common paint and equation (5) is used to calculate the contrast. The spectrum changes smoothly from absorption (when the plume is cold) to emission (when the plume is hot). At a temperature close to the zero-contrast condition, the spectrum is in emission at some wavelengths and absorption at others; here, a standard multiple regression fit will give zero concentration. Only when temperature-emissivity separation were being attempted would the chemical signature still be extractable from the data.
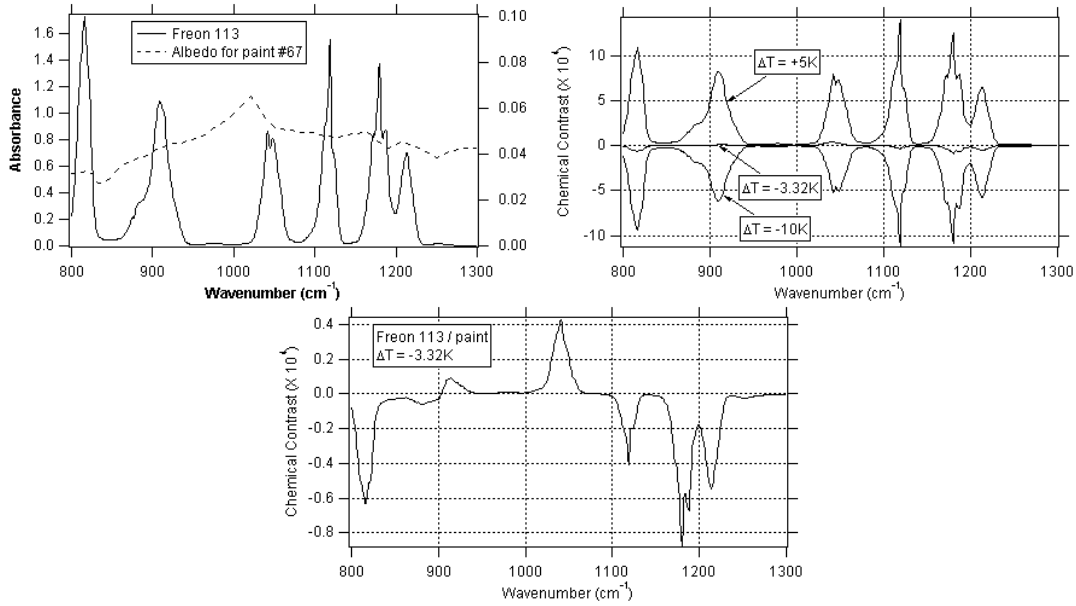
Figure 1. (top left) Spectrum of chemical and material. (top right) Chemical contrast $K(\nu,T_p)$ for the chemical and a single background material. Contrast spectra are plotted for different plume temperatures corresponding to plume absorption, near-zero contrast, and plume emission; $c_p l_p = 10^4$ ppm-m. (bottom) Expanded view of contrast spectrum near zero contrast. The chemical displays both emission and absorption features.

Chemical contrast in the plume signal is a function of three significant quantities:
- The chemical spectrum $\alpha(\nu)$
- The spectral albedo of the ground material $\varepsilon(\nu)$
- The difference in physical temperature between plume and ground, $\Delta T = T_p - T_g$.

Note that for a given chemical, the zero-contrast temperature ΔT_0 will occur at different places for different ground materials. This is because in Eqn. (5), the chemical spectrum $\alpha(\nu)$ acts as a set of weighting factors on the radiance difference $[L_p - \varepsilon L_g]$.

An illustration of the behavior of plume contrast with plume temperature is shown in Fig. 2. The chemical contrast, $K(\nu,T_p)$, was evaluated over a range of plume temperatures assuming some constant ground temperature. Only a single material is chosen for the calculation, as in Fig. 1. At each temperature, the spectrally dependent contrast was integrated over wavelength to give a net contrast, plotted in Fig. 2a. The resulting spectral signature was fitted to the chemical spectrum to give the fitted concentration in Fig. 2b. (For negative values of contrast, the absolute value of the fit is shown since concentrations must be non-negative.) The uncertainty in the fit is shown in Fig. 2c as a one-sigma value for the parameter standard deviation. Finally, Fig. 2d shows the uncertainty in the fit divided by the fitted concentration value, which corresponds to a noise-to-signal ratio. The minimum detectable concentration is related to this final quantity. The figure shows that over the temperature range of ~1 degree (-4.3 to -3.3 C), there is noise of ~5% and greater in detecting the chemical due to radiance contrast with the selected material.

In many chemical plume detection problems, the passive sensor must detect against a cluttered scene, in which the spectral albedo of the ground is different in each pixel. Suppose every pixel has the same physical ground temperature T_g. Since the zero-contrast temperature ΔT_0 is dependent on the material type, the value of the chemical contrast function (Fig. 2a) will vary from pixel to pixel. Even if the chemical concentration is the same across a group of pixels, the plume signature will vary in strength. This is how clutter adds noise to the detection problem.
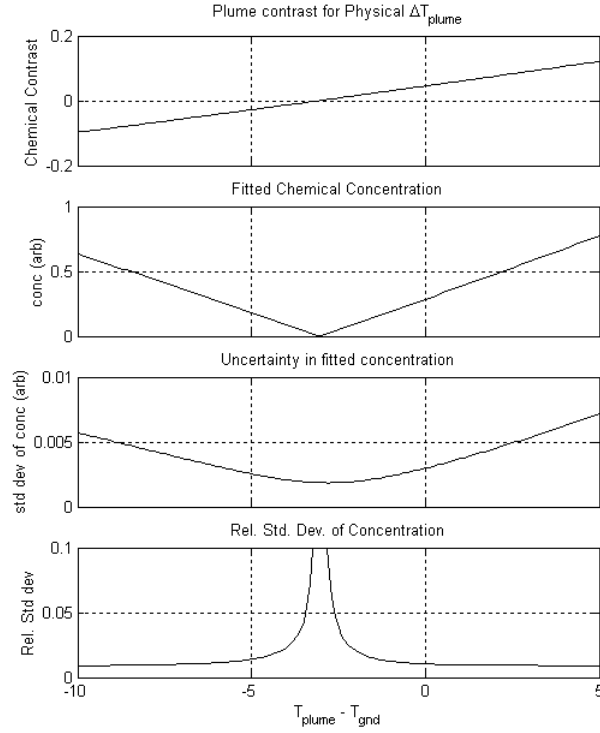
Figure 2. Plume contrast and detected concentration of chemical (in arbitrary units) as a function of temperature difference. Also shown are the uncertainty of a fit to the chemical in both absolute and relative terms.

From the foregoing discussion, it is clear that one could obtain improved chemical detection performance from a remote sensor by having knowledge of the ground temperature in a scene, its variation from pixel to pixel, and the spectral albedo in various pixels of the scene. Use of an active sensor alongside the passive sensor offers reflectivity information, which can be converted to emissivity and help to separate temperature from emissivity. In addition, a passive sensor could be used to identify on-plume and off-plume pixels with the same spectral albedo, enabling one to position the beam spot in appropriate places to "de-clutter" the active measurement as well. The intriguing capabilities of a hybrid system lead us to the experiments described next.

There are other noteworthy implications of radiance contrast. Since the zero-contrast temperature ΔT_0 is a function of both chemical and surface albedo, interesting things can happen when trying to detect two chemicals simultaneously in a plume. It is possible the physical temperature difference T_p-T_g at an on-plume pixel will be such that one chemical is detectable while the second is not. Alternatively, one chemical may appear in emission while the second is in absorption, even though their physical temperatures are identical. Finally, if T_p-$T_g \approx \Delta T_0$ for an unknown chemical, the chemical contrast may distort the chemical signature as shown in Fig. 1c to make it look like a different chemical. This is the condition for false-positive detection. All of these effects are directly traceable to the wavelength dependence in the radiance contrast $C_R(\nu)$. Approximating $C_R(\nu)$ by its wavelength-independent analogue C_B, as is often done by practitioners, will cause one to miss these phenomena.

3.0 EXPERIMENT DESIGN AND CONDITIONS

The instruments used in these experiments have parameters shown in Table 1. Hyperspectral passive images were taken by an instrument provided by Aerospace Corp. The CO_2 laser active system has been described previously.[8] We also obtained passive images from a separate sensor that utilizes a tunable Fabry-Perot filter and array detector. The latter instrument is under development at LANL and was used here primarily for lidar diagnostics. Results may be published

in the future. There are some significant differences in operating parameters between the passive dispersive instrument and the lidar instrument that complicate comparisons. The passive has better spectral coverage than the active, covering the full LWIR window, but somewhat lower spectral resolution. The spot size of the active instrument (i.e. the beam divergence) was about 3 times smaller than the passive, due to the imaging optics employed. The lidar instrument generates images by scanning a gimbal mirror. Slow movement of the mirror limits the size of images to 20 X 20 pixels as a practical limit. Many of these instrument parameters could potentially be made equal by further system development.

 The experiments were carried out over a two week period in early June of 2001 at a well instrumented lidar test range in Los Alamos. The general experimental conditions were those expected for a high desert environment in early summer. While generally the relative humidity was low (<30%), occasional thunderstorms would produce locally moist conditions for short times. Objects found in the images consisted of buildings, target boards, and other man-made objects, as well as vegetation and terrain features found locally. Vegetation consisted primarily of pinyon, juniper and ponderosa trees along with various grasses and shrubs. Local rock types are primarily volcanic in origin and include pumice, tuff, rhyolite, and basalt. Data were collected under a variety of lighting conditions from cloudy skies to full sunlight, and from the pre-dawn period to post-sunset. Ranges to most of the targets of interest varied from 1-6 km, but the full passive images viewed landscape features as far as 20 km and open sky. Simultaneous images were obtained for the active and passive systems at several locations at different times of day. "Staring" data was also obtained on selected objects in the scene. One of the target boards is a rough aluminum surface (sand-blasted aluminum) with reflectivity of ~80%, which serves as a calibration target and consistency check.

Chemical detection experiments were also carried out using a plume generator with known flow rates of gases, but the results are not discussed here.

Table 1. Instrument parameters

	Passive Dispersive Spectrometer	Active (CO_2 Lidar) System	Fabry-Perot Spectrometer
Detector	128 X 128 Array	Single-element HgCdTe	256 X 256 Array
Spectral coverage	128 channels 7.5 to 13.5 μm	44 channels 9.2 to 10.7 μm	Tunable 8 to 11 μm
Spectral Resolution	12 to 2 cm^{-1}	1.1 to 1.9 cm^{-1}	7 to 10 cm^{-1}
Field of View	1.11 mrad/pixel	0.35 mrad/pixel	0.015 mrad/pixel
Image sizes	128 X 300, 128 X 1300	20 X 20	256 X 256
Lidar parameters		0.7 mJ/pulse 5000 pps mirror scanned	

4. RESULTS AND DATA ANALYSIS

Results discussed here are only of a preliminary nature; we hope to do more detailed studies in the future. The focus for this paper is on comparing radiance and reflectivity spectra and looking for correlations. Also, we examine temperature dependences in the passive data because they are relevant to complications imposed by radiance contrast.

Figure 3 shows typical scene imaging data. Broadband images were constructed from both the passive and active data and are compared to an ordinary photograph. Although the spatial resolution of the images is much reduced from the photograph, one can make out the outlines of buildings and vegetation in each image. The data were also processed by K-means clustering to produce cluster maps shown in the figure. The major features in the scene generally show up in different clusters, although in the passive image the building at left is somewhat obscure. By examining other data like this, we have found that K-means clustering of the passive data tends to group together pixels of different brightness temperatures. There also seems to be a segregation according to atmospheric path length. Differences in spectral emissivity seem to be only a minor contributor to the cluster result.

Broadband Image

Broad-band image: 010609.005852.std

D06-010609-005801-tritium-t-l.cspe
Cluster Analysis Image

Cluster image: 010609.005852.std

D06-010609-005801-tritium-t-l.l2s

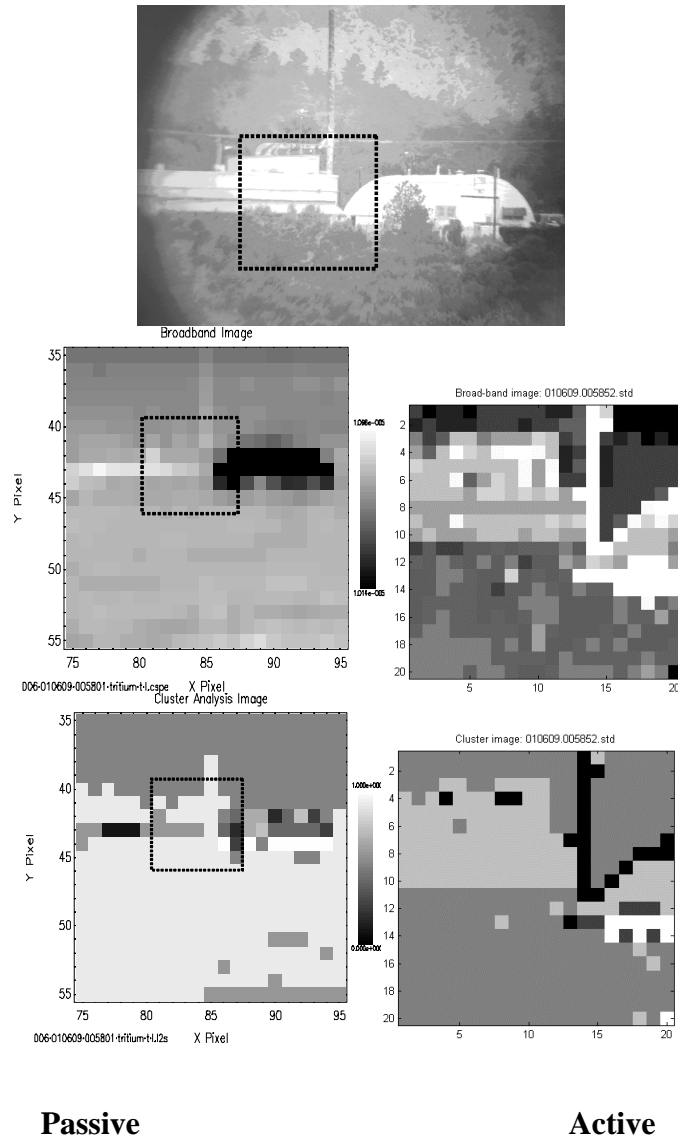**Passive**   **Active**

Figure 3. Scene images. (a, top) Photograph of area with buildings and trees. (b, second row) Passive broadband image (left) and active broadband image (right). (c, bottom row) K-means clustering maps of the passive data and active data. The dotted-line square in each case represents the area scanned by the lidar.

Figure 4 shows a series of cluster maps of the passive data through the day that help to explain why some objects are difficult to locate in the passive data. As object temperatures warm up in the sunlight, the radiance contrast between objects changes in a way that can make a given object either appear or disappear into its surroundings. The right-hand rectangle in the images in Fig. 4 demarcates a water tower in this scene. It is brought out in the cluster maps in the first and third images, but not in the second and fourth. The left-hand building is easiest to see in the second image, but somewhat obscure in the others. As the temperature distribution in the scene changes through the day, the radiance contrast is dramatically affected. This implies that the radiance contrast for a chemical plume would be similarly affected if it were situated in this scene.
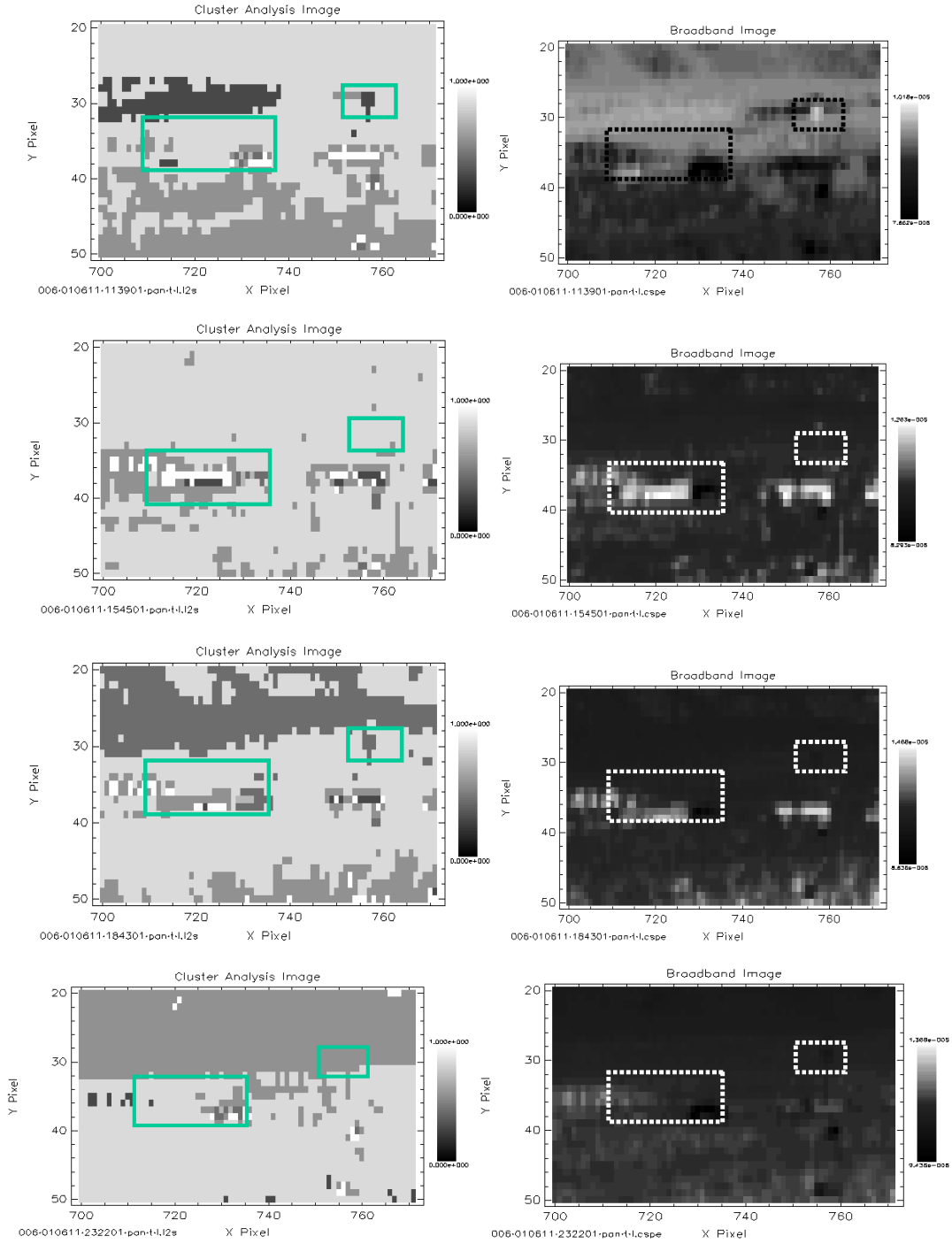
Figure 4. Evolution of cluster maps (left) and broadband images (right) from pre-dawn (top) to late afternoon (bottom). The scene contains buildings, trees, a watertower, and other objects.

Figure 5 illustrates how the lidar data can be calibrated. We used a sand-blasted aluminum target board at a range of 1.76 km. Previous work[12] indicates that the reflectance of this material is spectrally flat from 9-11 µm with R ≈ 45%. Weathering may have altered the absolute reflectivity somewhat. A flame-sprayed aluminum target board was determined to have the same spectral shape. We calculated a typical atmospheric transmission curve for the appropriate

atmospheric path. The lidar data are made to fit this curve by assuming that the instrument response function is a slowly varying polynomial, shown in the plot. It appears that the accuracy of this procedure is ~10%. Note that low signal is received at 976 cm^{-1} due to a very narrow water absorption feature.
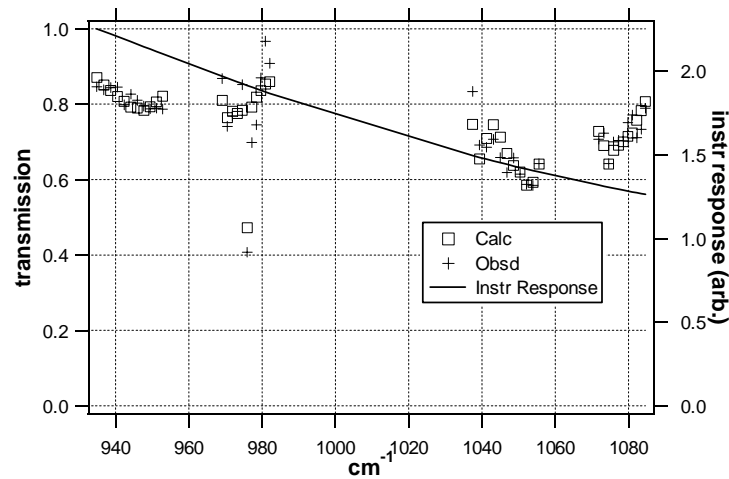

Figure 5. Calibration of lidar return data. The calculated points are from a model using range (1-way) = 1.76 km, 20% relative humidity, and appropriate atmospheric composition and conditions. The observed data are from a sand-blasted aluminum target, which was multiplied by the calibration curve shown to account for overall instrument response.

Figure 6a shows the passively detected radiance spectra for several objects in one scene that were obtained before dawn. Also shown is a calculated blackbody curve using Equation 4. A simple assumption to make is that at this time of day, all objects have the same temperature. If that is the case, we can obtain emissivity spectra for each by dividing out the blackbody curve shown in the figure. This procedure produces the "apparent emissivity" curves in Fig. 6b. The blackbody temperature of 295 K was deliberately chosen to yield an average emissivity of the rocks of about 0.92, which corresponds to the lidar measurement of ~8% reflectivity. For the low-emissivity objects, the detected radiance is dominated by atmospheric path emission and reflected radiance rather than the object itself. This is seen clearly by the ozone features in the spectrum that project upward. The "apparent emissivity" is then characteristic of the atmosphere, not the object. The aluminum target is known to have an emissivity of 1-0.80 = 0.20. In the figure, its apparent emissivity is much higher. The failure to obtain the correct value illustrates that atmospheric compensation must be included to obtain good correlation between active and passive spectra. This is especially true for high-reflectance (low emissivity) objects.

The assumption that different scene objects are at equal temperatures is simplifying but obviously too restrictive. An improved procedure from the above is to ratio the radiance curve for a given object to a blackbody curve of variable temperature, and attempt to match the result with the lidar-determined reflectivity. The results are plotted as spectral reflectance curves in Figure 7. Ideally, the curves should be the same. The data indicate that some features in the spectra are similar, but in many cases they conflict. In particular, the lidar spectrum of the rock (Fig. 7b) has a pronounced increase from 950 to 1050 cm^{-1} that is not present in the passive spectrum. We are currently trying to find the cause of the discrepancy. Clearly, the neglect of atmospheric compensation is a problem, but it is surprising that this should be so important for a ~1 km atmospheric path. The expected atmospheric transmission at this range is ~0.75-0.92 for CO_2 laser lines, depending on wavelength. Strictly speaking, Kirchhoff's Law relating emissivity to reflectivity (e = 1 – r) is valid only for hemispherical reflectance. The lidar measurement is a directional reflectance, and differences may also contribute to the observed discrepancy if the reflecting materials depart strongly from Lambertian behavior. Another problem in the comparison is the large difference in spot size or GSD of the two instruments. If the heterogeneity of the surface is large than expected, then the two sensors could be interrogating slightly different targets. More work is necessary to understand these comparisons.
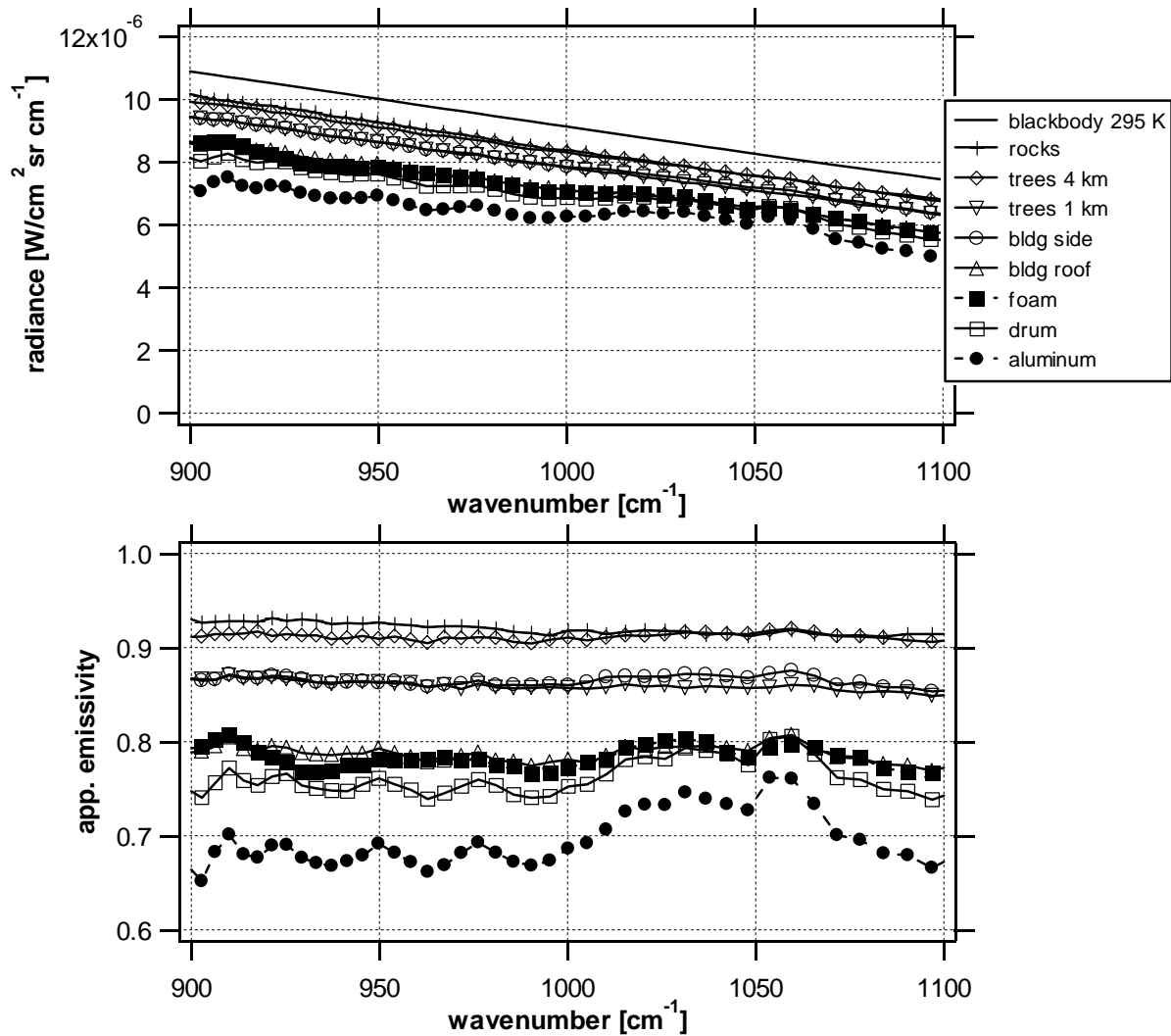
Figure 6. (top) Observed radiance spectra from the passive sensor. Also shown is a blackbody curve calculated for 295 K. The objects are various items located in the scene, both natural and man-made materials. (bottom) Spectra of "apparent emissivity" obtained by dividing the radiance spectra by the 295 K blackbody curve. Atmospheric ozone emission peaks are seen prominently in the aluminum and drum spectra, and less prominently in the other spectra.

SUMMARY

We carried out side-by-side measurements of a hyperspectral passive and multispectral active sensors. Images show many common features, as expected, but passive images can be difficult to interpret because of radiance contrast limitations and temperature-emissivity ambiguity. K-means clustering was used as a simple tool for preliminary analysis of the spectral images. As an image classification technique, it works reasonably well but appears to be influenced strongly by brightness temperature, whereas one hopes to classify the image according to spectral albedo. Together with differences in spatial resolution, image comparisons are somewhat difficult. We compared radiance and reflectivity spectra of individual scene objects. The expected correlations between spectral features were not always obtained. More sophisticated analysis employing atmospheric compensation may produce improved results in the future.
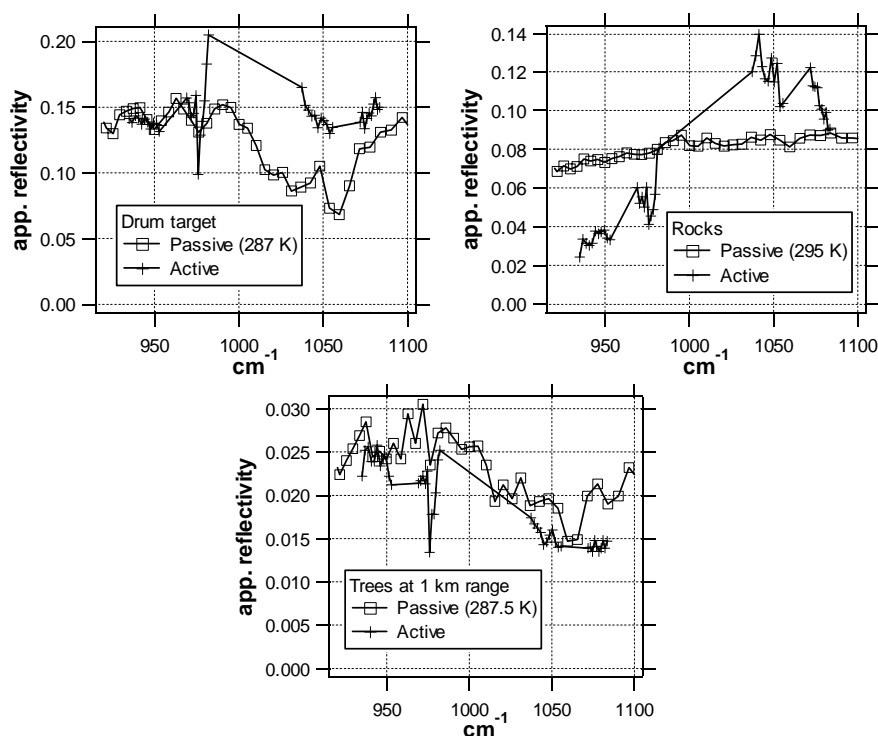
Figure 7. Comparison of active and passive spectra. For the passive, "apparent reflectivity" is one minus the "apparent emissivity" shown in Fig. 2. For each target, the passive spectra were ratioed to a blackbody curve (at the temperature shown) to give approximate agreement with the active average reflectivity.

ACKNOWLEDGEMENTS

REFERENCES

1. S.D. Kuo, J.R. Schott, and C.Y. Chang, "Synthetic image generation of chemical plumes for hyperspectral applications," *Opt. Eng.* **39**, p.1047-56, 2000.
2. S.D. Kuo and J.R. Schott, "Synthetic image generation of factory stack and cooling tower plumes," *Proc. SPIE* **3082**, p.175-86, 1997.
3. M.L. Polak, J.L. Hall, and K.C. Herr, "Passive Fourier-transform infrared spectroscopy of chemical plumes: an algorithm for quantitative interpretation and real-time background removal," *Appl. Opt.* **34**, p.5406-12, 1995.
4. D.F. Flanigan, "Detection of organic vapors with active and passive sensors: a comparison," *Appl. Opt.* **25**, p.4253-60, 1986.
5. D.F. Flanigan, "Prediction of the limits of detection of hazardous vapors by passive infrared with the use of MODTRAN," App. Opt. **35,** 6090-6098, 1996.
6. T. Hilgeman and L. Smith, "Advanced plume analysis software for gas measurement," Proc. SPIE **3082,** 128-135, 1996.
7. J. Sandsten, P. Weibring, H. Edner, and S. Svanberg, "Real-time gas-correlation imaging employing thermal background radiation," Optics Express **6,** 92-103, 2000.
8. B.R. Foy, B.D. McVey, R.R. Petrin, J.J. Tiee, and C.W. Wilson, "Remote Mapping of Vegetation and Geological Features by Lidar in the 9 -11 μm Region," *Appl. Opt.*, **40**, 4344-4352, 2001.

9. D.S. Lowe, "Effects of emissivity on airborne observation of roof temperature," Proc. Thermosense I (American Society of Photogrammetry), 1978. As quoted in J.R. Schott, *Remote Sensing: the Image Chain Approach,* pp. 209-210, Oxford University Press, New York, 1997.
10. A.B. Gschwendtner and W.E. Keicher, "Development of Coherent Laser Radar at Lincoln Laboratory," Lincoln Lab. J. **12,** 383-396, 2000.
11. A. Ignatov and G. Gutman, "Diurnal Cycles of Land Surface Temperatures," *Adv. Space. Res*. **22,** 641-644 (1998).
12. M.J. Kavaya, R.T. Menzies, D.A. Haner, U.P. Oppenheim, and P.H. Flamant, "Target reflectance measurements for calibration of lidar atmospheric backscatter data," Appl. Opt. **22,** 2619-2628, 1983.